JGR Planets

RESEARCH ARTICLE
10.1029/2022JE007426

Key Points:

- We propose an improved method to quantify impact-induced melt production for rocks
- We quantify impact-induced melt production and separate between heating due to shock compression and plastic work
- Melting due to frictional heating (plastic work) dominates over shock melting for impact velocities below 7–13 km/s depending on strength

Correspondence to:
L. Manske,
Lukas.Manske@mfn-berlin.de

Citation:
Manske, L., Wünnemann, K., & Kurosawa, K. (2022). Quantification of impact-induced melt production in numerical modeling revisited. *Journal of Geophysical Research: Planets*, *127*, e2022JE007426. https://doi.org/10.1029/2022JE007426

Received 9 JUN 2022
Accepted 10 NOV 2022

Quantification of Impact-Induced Melt Production in Numerical Modeling Revisited

Lukas Manske[1,2], Kai Wünnemann[1,2], and Kosuke Kurosawa[3]

[1]Museum für Naturkunde Berlin, Leibniz Institute for Evolution and Biodiversity Science, Berlin, Germany, [2]Department of Earth Sciences, Freie Universität Berlin, Berlin, Germany, [3]Planetary Exploration Research Center, Chiba Institute of Technology, Narashino, Japan

Abstract Melting and vaporization of rocks in impact cratering is mostly attributed to be a consequence of shock compression. However, other mechanism such as plastic work and decompression by structural uplift also contribute to melt production. In this study we expand the commonly used method to determine shock-induced melting in numerical models from the peak shock pressure by a new approach to account for additional heating due plastic work and internal friction. We compare our new approach with the straight-forward method to simply quantify melting from the temperature relative to the solidus temperature at any arbitrary point in time in the course of crater formation. This much simpler method does account for plastic work but suffers from reduced accuracy due to numerical diffusion inherent to ongoing advection in impact crater formation models. We demonstrate that our new approach is more accurate than previous methods in particular for quantitative determination of impact melt distribution in final crater structures. In addition, we assess the contribution of plastic work to the overall melt volume and find, that melting is dominated by plastic work for impacts at velocities smaller than 7.5–12.5 km/s in rocks, depending on the material strength. At higher impact velocities shock compression is the dominating mechanism for melting. Here, the conventional peak shock pressure method provides similar results compared with our new model. Our method serves as a powerful tool to accurately determine impact-induced heating in particular at relatively low-velocity impacts.

Plain Language Summary During the collision of cosmic bodies such as planets and asteroids on various scales, the involved material is heated such that melting or vaporization can occur. The vast amount of heat is considered to be generated during shock compression, however recent studies found that plastic deformation during decompression also contribute to the heating process. In this study, we introduce a new approach to quantify impact-induced melting more accurately under consideration of the latter heating mechanisms. We demonstrate that our approach is more accurate than previous attempts and quantify the contribution from plastic work on impact-induced melting. We systematically study the effect of impact velocity and material strength on melt production and find, that it is dominated by plastic work for impact velocities up to 7.5–12.5 km/s in rocks, depending on the material strength.

1. Introduction

The formation and evolution of Earth, the terrestrial planets, Moons, and other cosmic objects in the solar system has been significantly influenced by hypervelocity impact processes. Depending on the impact conditions, large quantities of impact-induced melt and vapor are generated. In previous studies melt production in impact events has been quantified mainly by semi-analytical models (e.g., Cintala & Grieve, 1998; Croft, 1982; Grieve & Cintala, 1992, 1997; Tonks & Melosh, 1993), and computer simulations using shock physics codes (e.g., Artemieva, 2007; Artemieva & Lunine, 2005; Barr & Citron, 2011; Bjorkman & Holsapple, 1987; Davison et al., 2010; Moreau et al., 2018; Nakajima et al., 2021; O'Keefe & Ahrens, 1977; Pierazzo et al., 1997; Wünnemann et al., 2008). The focus in most studies lies on the main heating and melting mechanism upon impact cratering, the shock compression. The passage of a shock wave increases the pressure temporarily, but causes permanent changes in density, internal energy, and entropy, giving rise to melting (Melosh, 1989; Zel'dovich & Raizer, 1969). If the shock-induced gain in internal energy and entropy is in excess of a critical amount the material will start to melt instantaneously or, most often, upon decompression to the initial pressure, as solidus temperature is a function of pressure. For simplicity the critical energy for melting E_M (e.g., Pierazzo et al., 1997) can be translated into a critical shock pressure for melting as end-member of the well-known progressive sequence of stages of shock metamorphism in rocks (e.g., Stöffler et al., 2018). In addition to shock compression, melting can also be

generated in impact cratering processes by the structural uplift of deep-seated strata that is decompressed upon its upward transport during the collapse of a transient crater resulting in the formation of complex crater structures (e.g., Ivanov & Melosh, 2003; Jones et al., 2005). Decompression melting is most relevant during large collision events in the early evolution of planetary bodies, which are thought to be initially much hotter than today giving rise to more efficient decompression melting. However, decompression does not contribute to the heat production by impact and, although our method is able to account for it (Manske et al., 2021), we neglect decompression melting here. The third melting mechanism upon impact is plastic work. Shock physics codes consider the resistance of matter against plastic deformation and, thus, account for plastic work and its contribution to the energy budget and temperature (e.g., Collins, 2014; Collins et al., 2004). Its effect on impact-induced melting and heating has been studied recently (Kurosawa & Genda, 2018; Kurosawa et al., 2021; Quintana et al., 2015; Wakita et al., 2019, 2022). According to these studies the contribution of plastic work to impact-induced melting and heating is significant up to a certain impact velocity at about 10 km/s. At higher velocities shock-heating dominates and the effect of plastic work becomes more and more negligible the stronger the shock wave. Commonly used scaling laws to estimate melt production in impact events (e.g., Abramov et al., 2012; Bjorkman & Holsapple, 1987; Pierazzo & Melosh, 2000; Pierazzo et al., 1997) are based on numerical modeling where basically the amount of matter that experiences shock pressures in excess of the critical shock pressure for melting is determined. Consequently, the widely used so-called Peak shock Pressure Method (PPM, after Quintana et al., 2015) does not account for the effect of plastic work (Pierazzo et al., 1997) and neither do scaling laws. Thus, the conventional scaling laws tend to underestimate melt production in particular at low impact velocities, depending on the strength of the involved matter. A more direct and straight-forward approach to determine melting in numerical modeling is, to use the temperature that is calculated by an equation of state (EoS) from density and internal energy, including the contribution from plastic work, in a computational cell and compare it with the solidus temperature for a given pressure. In principle this can be done at any point in time in the course of crater formation; however, it is usually conducted at the end of a simulation when more-or-less a steady state is achieved and the main dynamic motions have ceased to account for decompression melting and late-stage pressure fluctuations. We refer to this approach to quantify melt production as Final Temperatures Method (FTM, after Quintana et al., 2015). However, this method suffers from artificial diffusion mainly caused by averaging out temperatures due to mixing within cells of the computational grid and advection across cell boundaries which may significantly affect melt quantification (Artemieva, 2007). We further elaborate on problems inherent to the two methods in Sections 3.1 and 3.2.

To quantify melt production more accurately, we introduce an update of the PPM to account for plastic work besides shock heating and decompression melting (Manske et al., 2021). We describe the approach of our new method and compare it with results from previous studies using the FTM. With our new approach, we can quantify the contribution of heating due to plastic work on melting in more detail and compare it with the contribution from the shock wave. We do not take porosity into account in our study, but the proposed approach is also applicable to porous materials. Finally, we further investigate the effect of the impact velocity and material strength on melt production.

2. Method

We implemented our new approach to determine the contribution from plastic work in the iSALE-2D shock physics code (e.g., Amsden et al., 1980; Collins et al., 2004; Melosh et al., 1992; Wünnemann et al., 2006) in combination with the analytical equation of state (ANEOS) (Melosh, 2007; Thompson & Lauson, 1972). Minor changes in a few subroutines of the iSALE source code (see Data Availability Statement) could be implemented basically in any shock physics code that allows for recording the necessary thermodynamic properties by tracers. In all impact scenarios we present in the following, we assume a dunitic composition pertaining to both target and projectile and calculate the thermodynamic state of matter by the ANEOS for dunite (Benz et al., 1989). The elastic-plastic material response against deformation is considered by a strength model, more specifically by the so-called "ROCK" model (Collins et al., 2004). In this model, the yield strength is defined as:

$$Y = (1 - D)Y_{\mathrm{i}} + DY_{\mathrm{d}},$$

where Y_{i} and Y_{d} are the yield strength for intact and damaged material, respectively, and D expresses the damage the material experienced resulting in a reduction of strength. $D = 1$ correspondes to the maximum degree of damage and $D = 0$ the fully intact state. Following Kurosawa and Genda (2018) we neglect Y_{i} since the damage

D immediately reaches $D = 1$ upon shockwave arrival in areas where significant heating by plastic work can be expected. The yield strength for damaged material is defined according to the Drucker-Prager dry-friction law:

$$Y_{\mathrm{d}} = \min\left(Y_0 + \mu P, Y_{\mathrm{lim}}\right)$$

Here, Y_0 describes the materials cohesion, μ the friction coefficient, P is the pressure, and Y_{lim} the von Mises plastic limit which coresponds to the the yield strenght at infinite pressure. Furthermore, the material's strength depends on its temperature, as the shear strength drops to zero when approaching the solidus temperature (Ohnaka, 1995).

We use Lagrangian tracers to track the thermodynamic state the material experiences due to shock and plastic deformation. Massless Lagrangian tracers are placed initially in each computational cell of the Eulerian grid to represent the material within it. With the start of the simulation, the tracers move according to the velocity field in each computational timestep. As time progresses the tracers record the changes of physical properties within the cells that they pass such as pressure P and specific entropy S. The detailed procedure to estimate the total melt production is presented in detail in the next section.

3. Melt Quantification

In numerical models of impact cratering the thermodynamic state of material is described by state parameters such as temperature T, pressure P, specific entropy S, density ρ, and specific internal energy E that are linked to one another through an EoS. Depending on the EoS the melt temperature as a function of pressure is also provided; however, in this study we define solidus and liquidus temperature as a function of pressure independent from the EoS. Often shock physics codes do not record and track whether material is in solid, liquid or vapor state. At the end of a simulation—the end does not necessarily mean the end of crater formation—the thermodynamic state in each computational cell or tracer is evaluated to determine whether material is molten. In this section we summarize two commonly used approaches that come with advantages and disadvantages. Furthermore, we modified one of the methods in order to eliminate some shortcomings.

3.1. Final Temperature Method

A simple and straightforward approach to quantify impact-induced melting is to compare the final temperature in a cell or a tracer at the end of the simulation with the melt temperature taking into account the given ambient pressure. The so-called Final Temperature Method (FTM; Quintana et al., 2015) also accounts for heating by plastic work in addition to pure shock heating. Instead of temperature we use the specific entropy S that corresponds to the given temperature, specific internal energy E, and pressure P to ease the comparison with our improved approach (see Section 3.3). In addition, we record the entropy in a given cell by tracers which enables us to track the provenance of the molten material. Calculated results by the FTM via tracers and cells do not produce significant differences.

The problem of the FTM method is that it is grid-based. It relies on the thermodynamic state of a given cell. Since material is advected from one cell to another the thermodynamic state parameters suffer from artificial numerical diffusion. Numerical diffusion is a consequence of the transport of mass and energy through the grid of cells that is fixed in space, which results inevitably in an artificial dilution of strong gradients. Higher-order numerical solution schemes diminish numerical diffusion, but the longer the simulation and the more numerical iterations take place and the more mass and energy is advected, the stronger gradients and localized peaks in temperature and other state parameters are diluted and smeared out. The effect of numerical diffusion on melt production may be less problematic at early stages of crater formation, approximately up to the formation of the transient crater, but become more severe and lead to significant inaccuracies until the final or steady state of the crater is reached.

3.2. Peak Shock Pressure Method

To avoid numerical diffusion, a common approach uses the peak shock pressure recorded via tracers to determine melting in numerical modeling of impact cratering (e.g., Artemieva & Lunine, 2005; Pierazzo et al., 1997; Wünnemann et al., 2008). The so-called PPM takes advantage of the fact that shock melting occurs if the maximum shock pressure the material experiences is in excess of a certain critical pressure, which depends on the material and its condition (e.g., Liu et al., 2022; Manske et al., 2021). This critical shock pressure corresponds

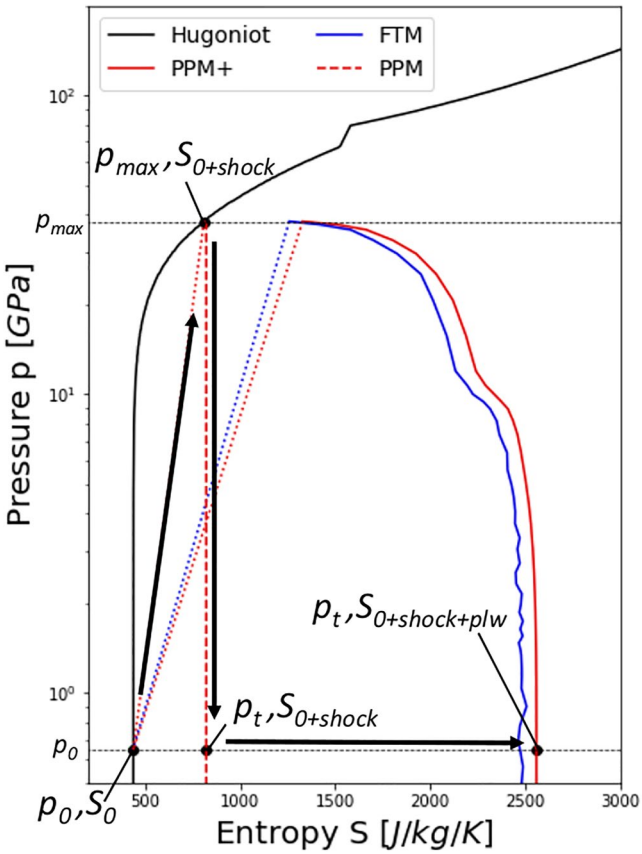

Figure 1. Schematic thermodynamic part either recorded by the tracer according to the final temperature method or recalculated according to the Peak shock pressure method (PPM, PPM+). The Hugoniot data is calculated after Benz et al. (1989) for $T_0 = 298$ K and $p_0 = 1$ atm.

to a certain increase in entropy, which indicates melting. The PPM implicitly assumes that the entropy once risen by shock compression does not change during decompression, namely, adiabatic expansion. To calculate the melt production, the method uses a material-based Lagrangian approach by introducing tracers that represent the material of the cell they were initially placed in and record the peak shock pressure and other physical properties the material experiences throughout the simulation.

3.3. A Modified Peak Shock Pressure Method

We extend the PPM to account for heating due to plastic work. To achieve this goal, we additionally implement the ability of tracers within the iSALE simulations to record the material's specific internal energy increase by plastic work E_{plw}. In other words, a certain tracer accumulates the plastic work of all computational cells it passes in the course of crater formation. Here, we describe the key modifications required to account for the contribution of plastic work to the total heat generated by impact in shock physics codes. The specific internal energy dissipated due to plastic work E_{plw} at a given time can be described as:

$$\frac{DE_{\mathrm{plw}}}{Dt} = \frac{1}{\rho} s_{ij} \dot{\epsilon}_{ij} \text{ for } \sigma_v (s_{ij}) > Y$$

Here, s_{ij} is the deviatoric stress tensor, $\dot{\epsilon}_{ij}$ describes the strain rate, and ρ is the materials density. σ_v corresponds to the equivalent von-Mises stress which is calculated via the second invariant of the stress tensor and describes the transition from elastic to permanent plastic shear deformation if it exceeds the yield strength Y. In the numerical simulation, we accumulate the specific internal energy by plastic work E_{plw} for a given tracer i and timestep n as follows:

$$E^{n+1}_{i,\mathrm{plw}} = E^{n}_{i,\mathrm{plw}} + \frac{s^n_{ij}}{\rho^n} \dot{\epsilon}^n_{ij} \Delta t$$

By additionally recording the tracers final pressure P_t and the peak shock pressure P_{max}, we reconstruct the material's thermodynamic path using the EoS (ANEOS). Note, this is a post processing procedure after the simulation is finished and P_{max}, P_t, and E_{plw} are known for each tracer. Figure 1 shows an example of an arbitrary tracer in P–S space.

First, we calculate the Hugoniot curve corresponding to the materials initial thermodynamic condition (P_0, S_0). Then we work out the shock-induced pressure increase via the recorded peak shock pressure P_{max} and the initial pressure for a given tracer. This is done by reconstructing the Rayleigh line starting at the initial position in the P–S space to the point where P_{max} intersects the Hugoniot curve at (P_{max}, $S_0 + S_{\mathrm{shock}}$). This maximum shock state reveals the entropy increase due to the shock S_{shock}. In a second step we calculate the release path from this state to the final state (P_t, $S_0 + S_{\mathrm{shock}} + S_{\mathrm{plw}}$). Upon release we approximate the change in the thermodynamic state in two steps: first we use ANEOS to calculate the isentropic release path to the final pressure P_t (P_t, $S_0 + S_{\mathrm{shock}}$). Up to this point we do not consider any contribution from plastic work according to the method used in Manske et al. (2021). A pure isentropic release only holds true if the effect of plastic work is negligible. Therefore, we add the accumulated energy the tracer has experienced by plastic work E_{plw} in a second step and work out the final state along an isobaric path to account for the contribution of plastic deformation. When the energy is added, the material ends up at the final state where the entropy increase due to plastic work S_{plw}, which is determined by ANEOS (P_t, $S_0 + S_{\mathrm{shock}} + S_{\mathrm{plw}}$). Instead of using ANEOS, the thermodynamic path can be reconstructed by any other EoS. The energy contribution from the shock E_{shock} corresponds to the specific internal energy increase from the initial energy E_0 to the energy at the state where the material has decompressed isentropically to the initial pressure after experiencing the shock (P_0, $S_0 + S_{\mathrm{shock}}$). In the following we refer to PPM and PPM+ to indicate whether we neglect plastic work or take the contribution from plastic work into account.

3.4. Melt Quantification and Analysis

To determine impact-induced melting we compare the post-impact entropy to the critical melt entropy, which corresponds to the melt temperature. The melt fraction of the material represented by the corresponding tracer i is defined as follows:

$$\psi_i \begin{cases} 0, & (\forall S_i < S_S) \\ \left(\dfrac{S_i - S_S}{S_L - S_S}\right), & (\forall S_S < S_i < S_L) \\ 1, & (\forall S_L < S_i) \end{cases}$$

Here S, S_S, and S_L are the specific entropy, the entropy for incipient melting (solidus), and the entropy for complete melting (liquidus), respectively. In the frame of this work, we do not distinguish between melting and vaporization. If the entropy is in excess of S_L the material is treated as superheated melt. The post-impact entropy S can be determined through the FTM, PPM, and PPM+.

The total impact-induced melt production is evaluated by the melting efficiency π_m, which is defined as the total melt volume normalized by the impactor volume V_p:

$$\pi_m = \frac{\Sigma_i \psi_i \cdot V_i}{V_p}$$

Here, V_i is the volume each tracer i represents, which corresponds to the volume of the computational cell the tracer was initially located in. ψ_i describes the degree of melting of the material represented by the tracer and varies between 0 (no melt) and 1 (complete melting).

The introduced method (PPM+) allows for quantifying the contribution of the different heating and melting processes. We do this by comparing the energy contribution from plastic work with the contribution from shock compaction. The ratio between plastic work and shock-induced internal energy for each tracer is given by:

$$\gamma_{\text{shock/plw}} = \frac{E_{\text{shock/plw}}}{E_{\text{shock}} + E_{\text{plw}}}$$

The method also enables to distinguish between the relative volumetric proportion of melting caused by plastic work $m^{\%}_{\text{plw}}$ or shock compression $m^{\%}_{\text{shock}}$:

$$m^{\%}_{\text{shock/plw}} = \frac{\Sigma_i \psi_i V_i \gamma_i^{\text{shock/plw}}}{\Sigma_i \psi_i V_i}$$

to quantify how much melt is produced due to the different heat mechanisms where $m^{\%}_{\text{plw/shock}}$ is 1 if the mechanism dominates and 0 if it does not contribute to melting ($m^{\%}_{\text{shock}} + m^{\%}_{\text{plw}} = 1$).

4. Impact Model Setup

To investigate the contribution from plastic work in impact-induced heating we carried out a systematic numerical modeling study. In our 2D vertical impact simulations we varied the impactor diameter L from 100 m to 50 km at a resolution, measured in cells per projectile radius, of 40. Furthermore, we varied the impact velocity v_i from 2.5 up to 35 km/s. According to the material model described above we define strength by a friction coefficient of $\mu = 0.6$ and cohesion of $Y_0 = 10$ kPa. To simulate different rock strengths, we vary the von Mises plastic limit Y_{lim} from $Y_{\text{lim}} = 0.5$–3.5 GPa. We further assume an Earth-like gravity of $g = 9.81$ km/s^2. To quantify the effect of plastic work on melting, we setup a simplified impact scenario, where we ignore pressure dependencies in the thermal profile and melt temperatures. Otherwise, the latter may lead to additional decompression melting, usually playing a role upon larger impact events (e.g., Manske et al., 2021). We assume a constant initial target and impactor temperature of $T_0 = 293$ K. The melt temperatures including the solidus and liquidus are set to $T_S = 1358.85$ (~2360) and $T_L = 2053.15$ K (~2845 J/K/kg), respectively, after Katz et al. (2003) at atmospheric 1 bar. This results in a melt energy E_M of 7.54×10^6 J/K, describing the specific energy of the shock

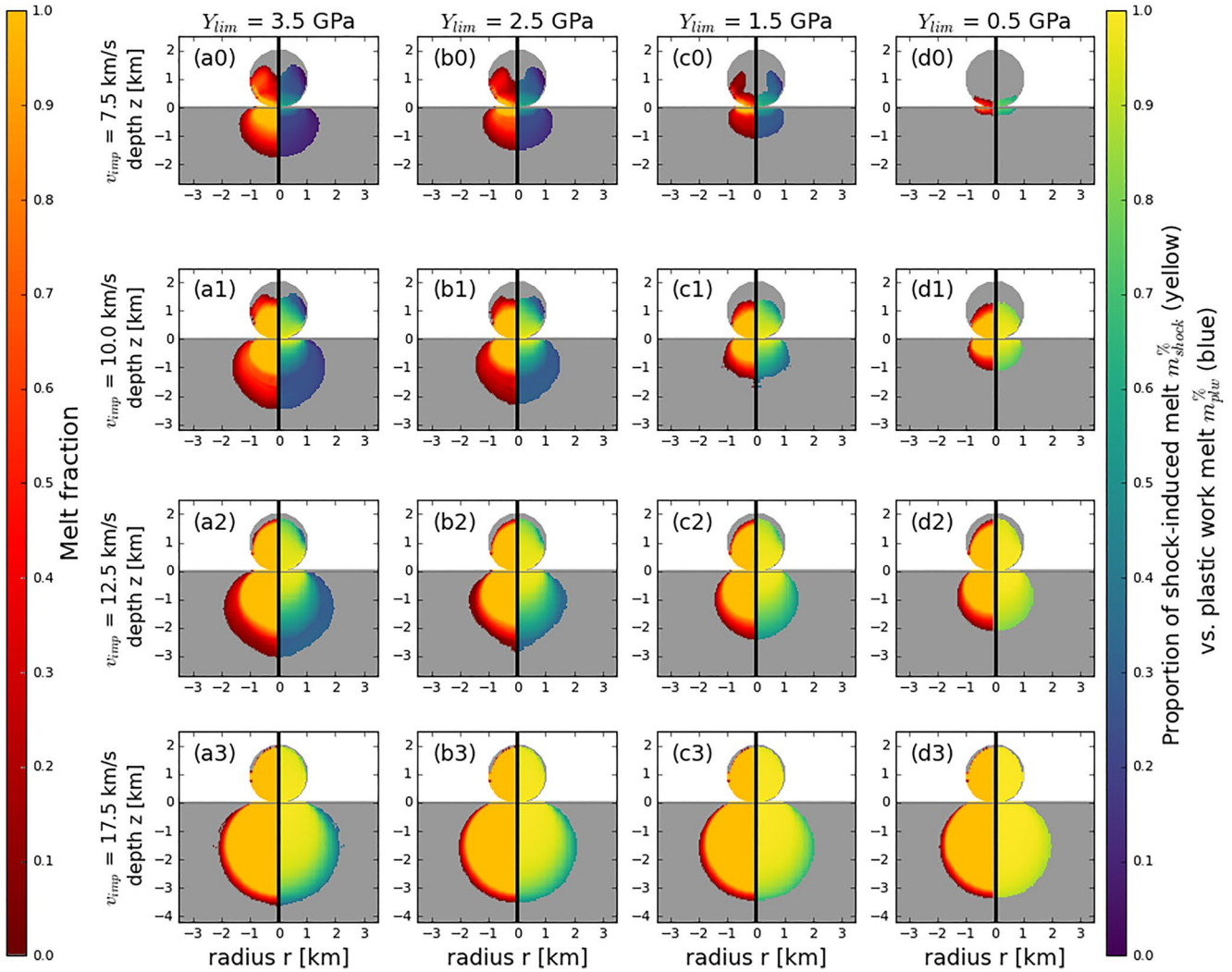

Figure 2. Melt contribution from plastic work in comparison to shock melting for varying impact velocities and strength (maximum strength Y_{lim}). The left panel of each frame shows the degree of melt (red incipient melting and yellow complete/superheated melt). The right panel shows, which heating mechanism is dominating (yellow corresponds to pure shock heating and blue corresponds to pure plastic work heating). Material is mapped back to its initial pre-impact position to ease comparison between different scenarios.

state (Rankine-Hugoniot state) from which the isentropic release ends at the liquidus at 1 bar (e.g., Bjorkman & Holsapple, 1987; Pierazzo et al., 1997).

5. Impact-Induced Melting as a Function of Velocity and Strength

The new PPM+ method enables us to distinguish between the different heating mechanisms, shock and plastic work. In this section we investigate the effect of velocity and strength on impact-induced melt production regarding both heating mechanisms. We expect that the impact velocity strongly affects the relative contribution of plastic work on impact melting, since the peak shock pressure of the shock wave is primarily controlled by the impact velocity. Therefore, low velocity impacts generate no or only a negligible amount of shock melting, while plastic work may still be sufficient to induce melting. In addition, how much heat is generated by plastic work depends on the strength of the material.

Figure 2 illustrates the melt fraction and the dominant mechanism of the melt production, which are mapped back to the pre-impact position as a function of strength and impact velocity. The lower the strength Y_{lim} of the material and the higher the impact velocity v_{imp} the less material is molten due to plastic work. For low impact velocities

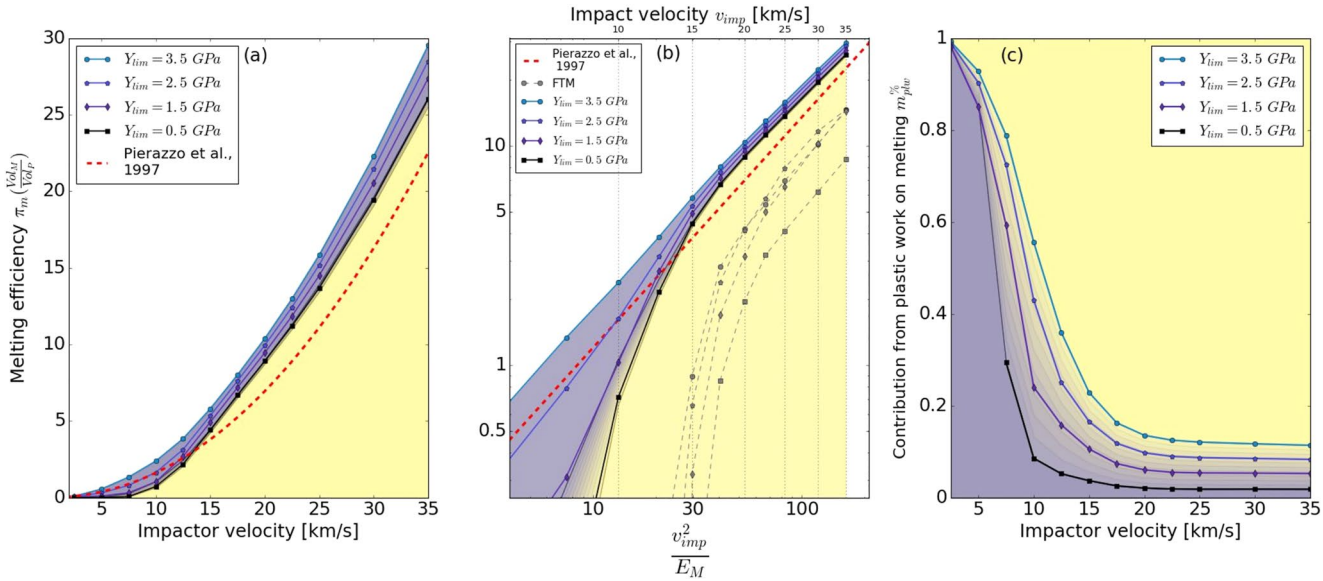

Figure 3. (a, b) Melting efficiency π_m and the contribution of plastic work on melting $m^{\%}_{plw}$ are plotted as a function of impact velocities and strength limits. Following Pierazzo et al. (1997), the melting efficiency is plotted against the melt number, v_{imp}^2/E_M, where the melt energy in the scaling-law is set to $E_M = 7.54 \times 10^6$ J/K (b). (a, c) The contribution from plastic work and shock melting is indicated with blue and yellow areas, respectively.

($\sim v_{imp} \leq 10$ km/s), heating due to the shock is less effective and the relative proportion from heating through plastic work is significant. With increasing impact velocity, the melt volume and the proportion of shock melting increases ($\sim v_{imp} > 10$ km/s). Here, shock melting dominates a circular area of the melt region emerging from the impact point, which corresponds to the material experiencing the highest shock. With increasing impact velocity, this area increases and eventually covers the whole melt area (e.g., Figures 2b0–3). The material in this area, which concentrically spreads out from the so-called "isobaric core," is predominantly completely molten and may be super-heated (c.f., Pierazzo et al., 1997). With increasing strength limit, melting due to plastic work dominates the outer part of the melt region, where pressures are too small to produce shock melt (e.g., Figures 2a–2d2). At first glance, the contribution to melting by plastic work may be negligible in some cases (e.g., Figure 2a3), but due to the cylindrical geometry, this area is large in volume. However, the produced melt at the rim of the melt region is mainly partially molten. At very low strength limits (Figure 2d, $Y_{lim} = 0.5$ GPa) the contribution from plastic work can be neglected. At low velocities, heating due to plastic work dominates the melt production. To narrow down the velocity where plastic work or shock dominates melting in more detail, we plot in Figure 3 melting efficiency and the contribution of both heating mechanisms as a function of impact velocity v_{imp} and the limiting strength Y_{lim}.

In general, our data agree with previous studies indicating that plastic work is the dominant heating process up to an impact velocity of approximately 10 km/s (Kurosawa & Genda, 2018). For higher impact velocities shock heating dominates melting. In more detail we find that the contribution from shock on melting efficiency for dunite under earth-like surface conditions ($T_0 = 298$K and $p_0 = 1$ atm) is negligible for impact velocities up to 7.5 km/s (c.f. Figure 3, left plot). Up to this threshold velocity, impact-induced melt is produced only at strength limits larger than 0.5 GPa and is dominated by heating due to plastic work. With increasing velocities, material strength affects the total melt production $m^{\%}_{plw}$, depending on the materials yield strength (Figures 3a and 3c). While for a low yield strength limit of $Y_{lim} = 0.5$ GPa no significant melt due to plastic work is produced. A large strength limit of $Y_{lim} = 3.5$ GPa results in a contribution of plastic work on the total melt production of about 35% at a velocities of 12.5 km/s. At velocities higher than about 20 km/s, the contribution from plastic work becomes constant for increasing impact velocities, independent of the strength limit Y_{lim}. Here, roughly 12% of the melt is still produced by plastic work at a strength of $Y_{lim} = 3.5$ GPa. This contribution subsequently decreases with decreasing Y_{lim} and can be neglected in case of the lowest strength of $Y_{lim} = 0.5$ GPa.

We further compare our data with the scaling law for dunite from Pierazzo et al. (1997), which is based on the PPM and thus only accounts for shock heating (Figure 3b). The scaling law approximately fits the data for

high velocity impacts of 17.5 km/s or greater. The fact that the scaling law slightly underestimates our data for high velocities emerges from the consideration of partial melting, while the scaling law only accounts for the liquidus (E_M), that is, complete melting. Here we adjusted the melt energy of the scaling law E_M (from originally $E_M = 9 \times 10^6$ to $E_M = 7.54 \times 10^6$ J/kg) according to the liquidus function and the EoS used in this study (from originally $S_L = 3240$ to $S_S = 2845$ J/kg/K), however the effective melt energy in our simulations is reduced due to partial melting. In this velocity range, the increase in melt production with increasing strength Y_{lim} follows a constant behavior and can be expressed by a reduction of the melt energy E_M in the scaling law to account for plastic work (Pierazzo et al., 1997). For velocities lower than about 15 km/s however, melt production cannot be expressed by a power law anymore due to the breakdown of the point-source limit (e.g., Bjorkman & Holsapple, 1987; Pierazzo et al., 1997). Here the scaling law fails to give a reliable estimate and tends to overestimate melt production when the velocity further decreases and strength limits are low ($Y_{\text{lim}} \leq 2.5$ GPa). However, the scaling law fits the slope of the $Y_{\text{lim}} = 3.5$ GPa data, which we consider to be coincidental.

6. Discussion on Different Approaches to Quantify Impact Melting

The quantification of shock-induced melting in numerical modeling requires only a simulation time until the shock wave has attenuated below the critical shock pressure for melting. Relative to the total crater formation time, this is a rather short time period. Therefore, it is computationally rather inexpensive to determine the amount of shock melting. However, to track the distribution and final deposition of melt it is necessary to simulate the entire crater formation process. In addition, late-stage crater formation processes can cause additional melting due to plastic work, as shown above, and due to decompression (e.g., Ivanov & Melosh, 2003; Manske et al., 2021). In these cases, all Eulerian shock physics code, such as iSALE, suffer from artificial numerical diffusion the longer the simulation time and the more numerical iterations are calculated. Here we compare the different methodological approaches (FTM and PPM+, c.f. Method section) to determine melt production upon impact crater formation with respect to numerical diffusion.

Figure 4 illustrates the effect of artificial diffusion on the entropy field for FTM. For better comparison we use a similar setup as Kurosawa and Genda (2018) for the hydrodynamic (Figure 4c) and strength case (Figure 4b), including an Earth-like gravity. Furthermore we added a run with a smaller impactor diameter $L = 500$ m (Figure 4a) and tracked five selected tracers in each run according to the setup of Kurosawa and Genda (2018). We find that the FTM suffers severely from artificial diffusion if the impact-induced thermal anomaly experiences extensive displacement (advection) and stretching (c.f. Figure 4, left plots). This is the case when there is no strength present to resist the materials movement (Figure 4c) or if the impact-induced thermal anomaly is small relative to the transient crater (gray line). In the latter case, the thermal anomaly is stretched and advected beyond the transient crater's wall throughout crater formation (Figure 4a). Then, the potentially molten materials experience further advection during the collapse of the transient crater. However, if the thermal anomaly is generated to a significant extent outside of the transient crater volume, it is less displaced (Figure 4b) and the FTM still deliver acceptable results at the steady state. Compared to the PPM+, the FTM is not able to conserve the peak entropies that are produced in the early contact and compression stage (c.f. Figure 4, center and right column). This can be observed in the histogram and S–t plot where the Entropy calculated by the PPM+ stays constant after heating while the Entropy in the FTM is altered by diffusion with ongoing advection and time. In the histogram (Figure 4, center column), this is indicated by the thin dotted lines describing earlier timesteps, where the FTM and the PPM+ show similar entropy values. Depending on the case (Figures 4a–4c), the accumulated entropy calculated by the FTM may significantly change with ongoing time until the steady state is reached (thick dashed lines). In the FTM the peak entropy values are diluted compared to the PPM+ leading to heating of surrounding, initially colder material. In the S–t plot (right), the entropy recorded by the five selected tracers is strongly affected by artificial diffusion when using the FTM.

Figure 5 illustrates the melting efficiency π_m as a function of impact velocity for different impactor sizes determined by both methods, PPM+ and FTM. The yield strength Y_{lim} is 3.5 GPa. Also, the melt efficiency calculated via the PPM is plotted which does not align with the shock contribution from the PPM+ because additional melting partially due to the shock in the PPM+ emerges in combination with plastic work heating. In general, the melt production calculated by the PPM+ is not significantly affected by the impactor size. However, with increasing impactor size, gravity dominates the late-stage crater modification resulting in the formation of complex craters (e.g., $L = 50$ km). The more vigorous this late-stage modifications are, the more additional melt due to plastic

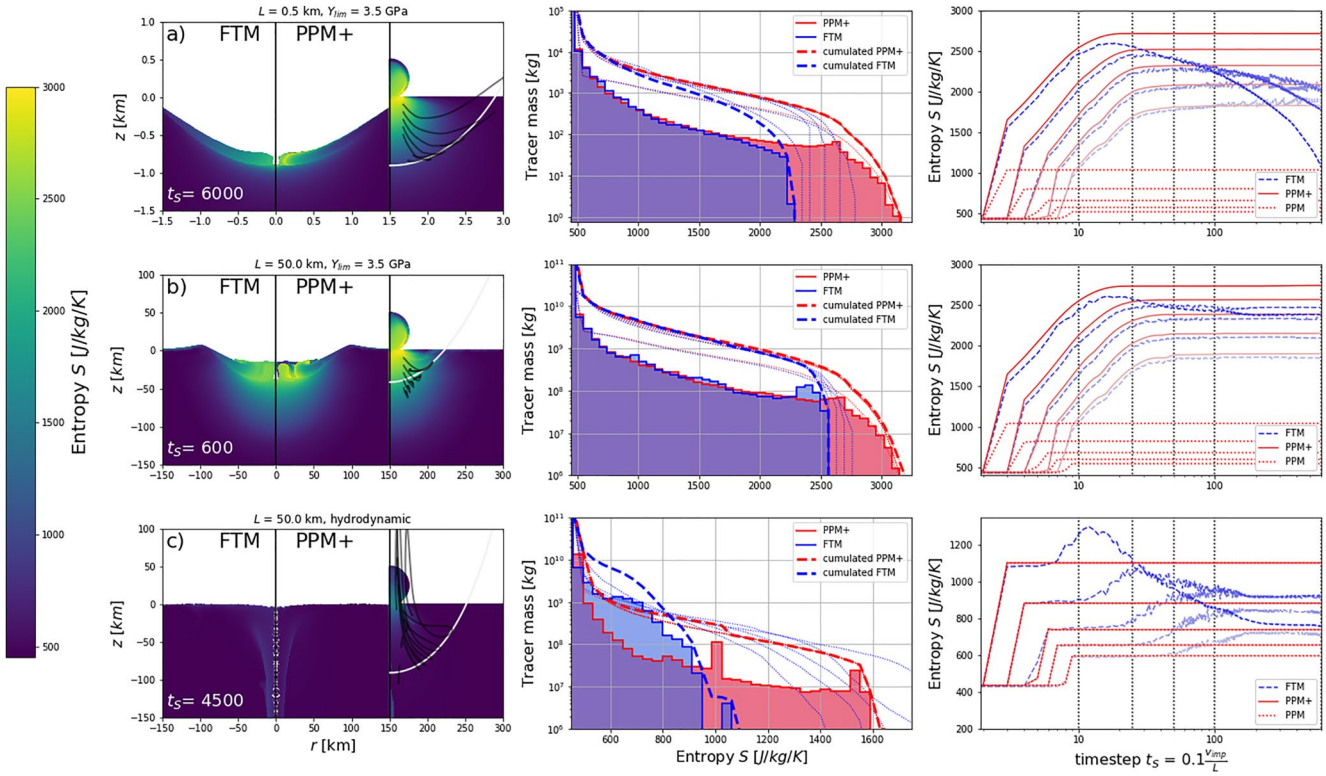

Figure 4. The evolution of entropy using Final Temperatures Method and PPM+ methods for three cases (a–c) with varying impactor size and strength with a resolution of 50 cells per projectile radius; Left column: entropy distribution for both methods at a 6 km/s. The trajectories of five selected tracers are indicated by black lines. Also, the PPM+ entropy distribution at the initial position is plotted in relation to the transient crater (light gray line, calculated after Manske et al. (2021)); Center column: Entropy according to the (accumulated) tracer masses plotted in a histogram illustrated by a solid line (dashed line) at the final state for both methods. The thinner dotted lines indicate accumulated entropies of previous timesteps (t_S = 10, 25, 50, 100, 600, where t_s is a characteristic time for projectile penetration); Right column: the selected tracer's changes in entropy which is increasing by the experienced shock pressure and plastic work while eventually being affected by diffusion with time.

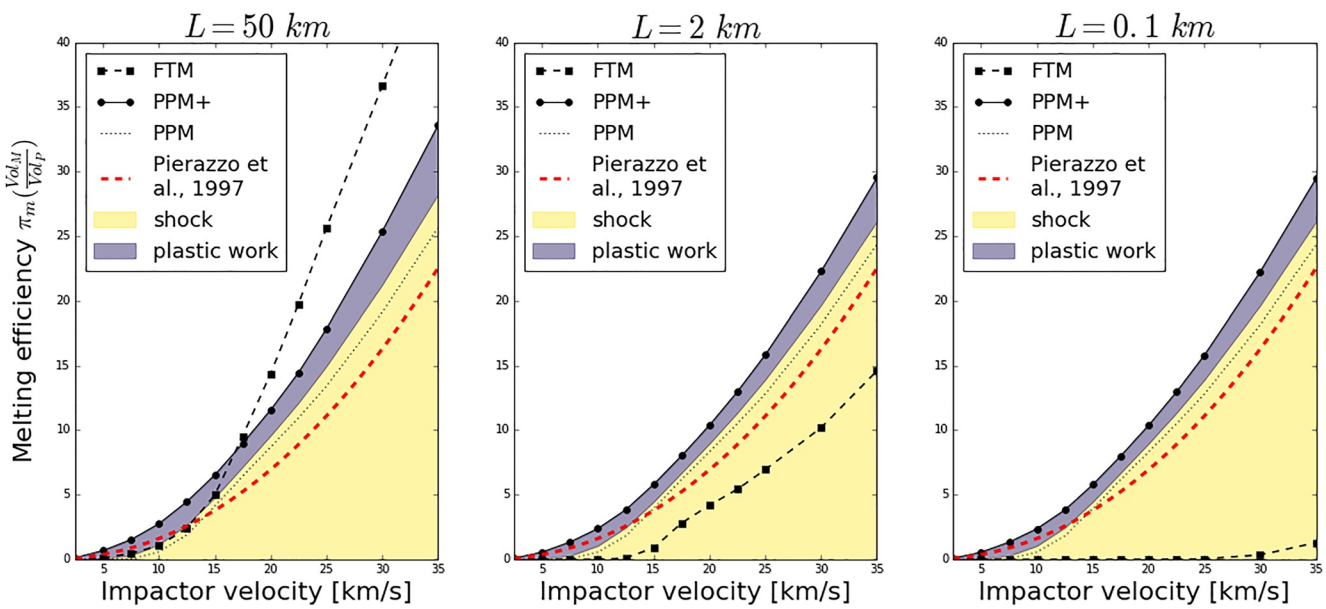

Figure 5. Melting efficiency π_m as a function of impactor velocity v_i for different impactor diameters L. π_m Was determined when the final crater was formed (steady state). The dashed red line indicates the melt scaling law after Pierazzo et al. (1997).

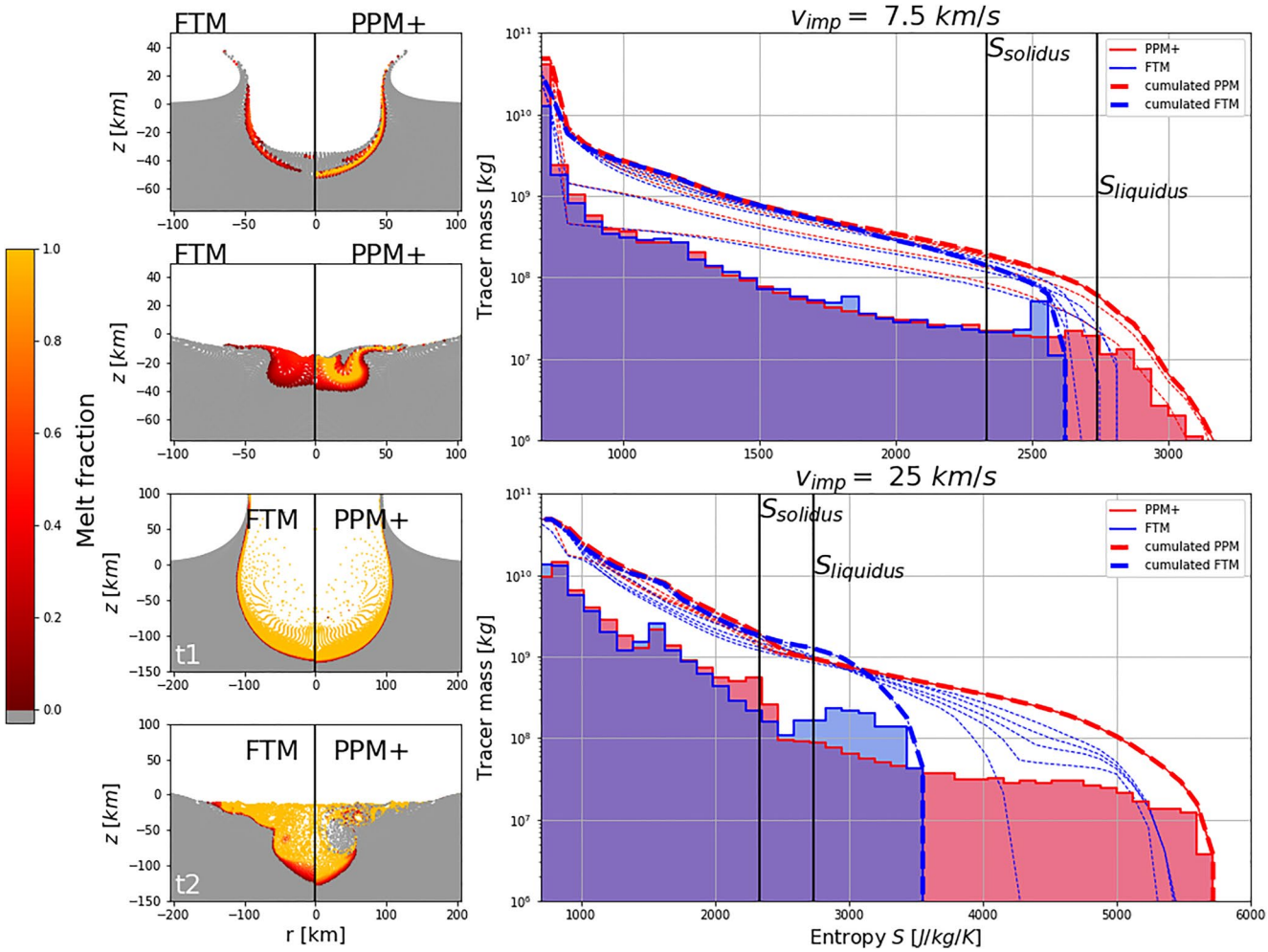

Figure 6. Melt distribution and tracer mass entropy histogram during crater formation for 7.5 and 25 km/s (early time step t_1 on top and steady/final state t_2 at the bottom). The vertical solid lines indicate the solidus and liquidus temperature, respectively. The thick dashed line and the histogram data describes the tracer's (accumulated) entropy at the final timestep t_2. The thin dashed lines indicate the tracer's cumulated entropy of previous timesteps.

work is produced. Comparing the FTM with the PPM+ reveals significant deviations in melt production at the final state. In case of a large impactor $L = 50$ km, melting efficiency is underestimated for lower impactor velocities at about 15 km/s and overestimated for impactor velocities of about 17.5 km/s. For the smaller impactors, melting efficiency is always underestimated. In the extreme case of $L = 0.1$ km, the majority of the melt is being ejected beyond the rim of the final crater. In this case, the temperature of the ejected material is significantly reduced due to diffusion during the advection and mixing with cold material in the computational cells outside the crater.

Deviations between both methods can be explained by dilution of the impact-induced thermal anomaly resulting from artificial numerical diffusion in the FTM. Numerical diffusion can cause both an increase or decrease in the melt production. It depends on how much the thermal anomaly is smeared out and mixes with the surrounding material and how the resulting temperature compares with melting temperatures. To quantify these competing effects, we plot in Figure 6 the tracer's entropy cumulatively in a histogram for different time steps (dashed and dotted lines). The figure illustrates how the tracer's entropy S_i calculated by the FTM and PPM+ change with time for different impact velocities, where impact-induced melt volumes are either over or underestimated. We choose an early simulation time during crater formation t_1 where most of the impact-induced heating is completed and a late simulation time t_2 when the steady state is reached, where the material barely moves anymore. In the PPM+ the tracer's post-heating entropy does not vary significantly with time. This, however, is not the case for the FTM, where artificial diffusion strongly effects the tracers' temperatures. At an early timestep t_1 and a low

impact velocity $v_{imp} = 7.5$ km, for a few tracers the impact-induced entropy slightly exceeds the liquidus entropy while for the higher velocity $v_{imp} = 25$ km, the thermal anomaly is even bigger. Along with the crater formation and increasing number of advection cycles at t_2, numerical diffusion dilutes the thermal anomaly in the FTM until the steady state is reached (dashed and solid lines). This causes the maximum entropy of the anomaly to decrease but also to distribute the heat to the surrounding material (energy is conserved, but distributed over a larger area). At low velocities, the thermal anomaly is too small and decreases more rapidly below melting entropy, which results in underestimating the total melt production. At higher velocities, the opposite is the case. Here diluting of a sharp large thermal anomaly rather causes colder surrounding material to be heated above melting temperature than cooling hotter material below melting temperature. This results in overestimating melt production.

7. Discussion and Conclusion

We have revisited the long-standing issue how to determine impact induced melt production in numerical simulations. We propose an update to the most widely used PPM to allow for taking into consideration the contribution from plastic work in addition to pure shock-heating. Based on a previous approach analyzing decompression melting (Manske et al., 2021) the presented method is capable to account for and quantify all relevant heating sources including shock, plastic work and with respect to melting also decompression melting as a consequence of structural uplift by a tracer-based method to avoid artificial diffusion of heat due to numerical advection errors.

In previous work Quintana et al. (2015) compared the FTM with the PPM. They found that the FTM produces similar results to the PPM, however the PPM fails to quantify impact-induced melt at impact velocity below 8 km/s, where peak shock pressures are insufficient to generate shock melting, but some melting results from plastic work as shown by Kurosawa and Genda (2018). Our data agrees with these findings, and we demonstrate that the PPM+ solves this issue. Previous studies also indicate that the impact velocity v_{imp} is the controlling parameter for the relative contribution from plastic work on impact melt production. We can confirm that a significant change occurs at a threshold velocity of about 10 km/s (Kurosawa & Genda, 2018) for dunite by quantifying the contribution of the shock and the plastic work to the melt production. The threshold velocity may vary depending on yield strength from 7.5 to 12.5 km/s for $Y_{lim} = 0.5$ to $Y_{lim} = 3.5$ GPa, respectively. At impact velocities below 17.5 km/s the contribution of plastic work almost linearly increases up to 100% at a velocity of 2.5 km/s. For impact velocities higher than 17.5 km/s and a high strength limit $Y_{lim} = 3.5$ GPa, the contribution from plastic work is rather low and makes up about 12% of the melt. This contribution may be negligible, especially for lower strength limits. In a more realistic scenario, where the temperature (and pressure) dependent strength decreases with depth, the contribution of plastic work will further decrease with increasing impactor velocity and diameter. This is, because such impacts transfer more of their kinetic energy deeper into the target, where strength is reduced by thermal softening (Ohnaka, 1995). Thermal softening reduces the strength as temperature approaches the melt temperature. Melt is treated strengthless and usually melt viscosity is neglected. At a low yield strength limit of $Y_{lim} = 0.5$ GPa, the contribution from plastic work is negligible. In this case and at high impact velocities $v_{imp} \geq 17.5$ km/s, melting efficiency approximately agrees with scaling laws (Pierazzo et al., 1997). For lower impact velocities, the scaling law fails to accurately fit the data and tend to overestimate the melt as if strength was applied, though the scaling law only applies for pure shock melting such as the original PPM approach (Pierazzo et al., 1997). This is due to fact that at such low melt numbers $v_{imp}^2/E_M \leq 30$ ($m^{\%}_{plw} \geq 0.5$), the minimum impact velocity where melt and vapor is generated is almost reached and the point source assumption break down (e.g., Bjorkman & Holsapple, 1987; Pierazzo et al., 1997). So, the scaling law fails at low velocities due to the extrapolation of high velocity data in the shock melting regime $v_{imp}^2/E_M > 30$ ($m^{\%}_{plw} < 0.5$). Here, the melt tends to be overestimated with decreasing velocity and the strength Y_{lim} ($Y_{lim} \leq 2.5$ GPa). For this reason, the usage of such scaling laws at low impact velocities has to be done with caution.

A similar behavior with respect to the strength parameters and the impact velocity can be expected for other materials, such as granite or basalt. The latter have slightly lower critical shock pressures than dunite (e.g., Stöffler et al., 2018). Thus, shock melting is more dominant and the threshold velocity, for the transition from plastic work-dominated to shock-dominated melting is expected to be smaller.

We demonstrate that the improved method (PPM+) is more robust against numerical diffusion than the intrinsic Final Temperature Method (FTM) if simulations are carried until late stages of crater formation and the final deposition of melt is of interest. In the early stage of the simulations the FTM mostly provides sufficiently accurate results of the total melt production, neglecting late-stage heating. However, the FTM suffers from artificial

diffusion in every timestep while significant heating due to plastic work (and the shock) happens over a longer period of time (c.f. Figure 4). Thus, the FFM should not be used in scenarios where strong diffusion (and thus temperature alteration) due to numerical advection errors is expected. This is often the case for simulations of late stages of crater formation, where it is necessary to consider plastic work and decompression melting during crater modification. The larger the transient crater is compared to the area of the thermal anomaly; the more advection is expected and the more the FTM may suffer from numerical inaccuracies (c. f. Figure 4). Also, the relationship of the amplitude of the thermal anomaly to the melt temperatures is important to monitor. When the thermal anomaly is small compared to melting temperatures (usually at low impact velocities; here $v_{imp} < 15$ km/s) artificial diffusion may lead to melt underestimation while for larger thermal anomalies (usually for high impact velocities; here $v_{imp} > 20$ km/s) the opposite is the case.

Data Availability Statement

The iSALE shock physics code is not entirely open-source but can be distributed on a case-by-case basis to academic users in the impact community for non-commercial use. Scientists interested in using the code find the application requirements at the iSALE website (http://www.isale-code.de/redmine/projects/isale/wiki/Terms_of_use). The ANEOS package comes along with iSALE. The modification in iSALE and the input files to generate the results supporting the figures are available in Manske et al. (2022), https://doi.org/10.35003/HVTJQD.

Acknowledgments
We greatly appreciate reviews from Meng-Hua Zhu and an anonymous reviewer for insightful reviews that improved the quality of the manuscript. We gratefully acknowledge the developers of pySALEPlot including Tom Davison and the developers of iSALE-2D, including Gareth Collins, Dirk Elbeshausen, Boris Ivanov, and Jay Melosh (www.isale-code.de). L.M. and K.W. are supported by the Deutsche Forschungsgemeinschaft (SFB-TRR 170, subproject C4). This is TRR 170 Publication No. 179. K.K. is supported by JSPS KAKENHI JP18KK0092, JP19H00726, JP21K18660, and JP21H01140. Open Access funding enabled and organized by Projekt DEAL.

References

Abramov, O., Wong, S. M., & Kring, D. A. (2012). Differential melt scaling for oblique impacts on terrestrial planets. *Icarus*, *218*(2), 906–916. https://doi.org/10.1016/j.icarus.2011.12.022

Amsden, A. A., Ruppel, H. M., & Hirt, C. W. (1980). *SALE: A simplified ALE computer program for fluid flow at all speeds* (No. LA-8095). Los Alamos Scientific Lab.

Artemieva, N. (2007). Possible reasons of shock melt deficiency in the Bosumtwi drill cores. *Meteoritics & Planetary Sciences*, *42*(4–5), 883–894. https://doi.org/10.1111/j.1945-5100.2007.tb01083.x

Artemieva, N., & Lunine, J. I. (2005). Impact cratering on Titan II. Global melt, escaping ejecta, and aqueous alteration of surface organics. *Icarus*, *175*(2), 522–533. https://doi.org/10.1016/j.icarus.2004.12.005

Barr, A. C., & Citron, R. I. (2011). Scaling of melt production in hypervelocity impacts from high-resolution numerical simulations. *Icarus*, *211*(1), 913–916. https://doi.org/10.1016/j.icarus.2010.10.022

Benz, W., Cameron, A. G. W., & Melosh, H. J. (1989). The origin of the Moon and the single-impact hypothesis III. *Icarus*, *81*(1), 113–131. https://doi.org/10.1016/0019-1035(89)90129-2

Bjorkman, M. D., & Holsapple, K. A. (1987). Velocity scaling impact melt volume. *International Journal of Impact Engineering*, *5*(1), 155–163. https://doi.org/10.1016/0734-743X(87)90035-2

Cintala, M. J., & Grieve, R. A. (1998). Scaling impact melting and crater dimensions: Implications for the lunar cratering record. *Meteoritics & Planetary Sciences*, *33*(4), 889–912. https://doi.org/10.1111/j.1945-5100.1998.tb01695.x

Collins, G. S. (2014). Numerical simulations of impact crater formation with dilatancy. *Journal of Geophysical Research: Planets*, *119*(12), 2600–2619. https://doi.org/10.1002/2014je004708

Collins, G. S., Melosh, H. J., & Ivanov, B. A. (2004). Modeling damage and deformation in impact simulations. *Meteoritics & Planetary Sciences*, *39*(2), 217–231. https://doi.org/10.1111/j.1945-5100.2004.tb00337.x

Croft, S. K. (1982). A first-order estimate of shock heating and vaporization in oceanic impacts. *Geological Implications of Impacts of Large Asteroids and Comets on Earth*, *190*, 143–152.

Davison, T. M., Collins, G. S., & Ciesla, F. J. (2010). Numerical modelling of heating in porous planetesimal collisions. *Icarus*, *208*(1), 468–481. https://doi.org/10.1016/j.icarus.2010.01.034

Grieve, R. A. F., & Cintala, M. J. (1992). An analysis of differential impact melt-crater scaling and implications for the terrestrial impact record. *Meteoritics*, *27*(5), 526–538. https://doi.org/10.1111/j.1945-5100.1992.tb01074.x

Grieve, R. A. F., & Cintala, M. J. (1997). Planetary differences in impact melting. *Advances in Space Research*, *20*(8), 1551–1560. https://doi.org/10.1016/s0273-1177(97)00877-6

Ivanov, B. A., & Melosh, H. J. (2003). Impacts do not initiate volcanic eruptions: Eruptions close to the crater. *Geology*, *31*(10), 869–872. https://doi.org/10.1130/G19669.1

Jones, A. P., Wünnemann, K., & Price, D. (2005). Modeling impact volcanism as a possible origin for the Ontong Java Plateau (OJP). In G. R. Foulger, J. H. Natland, D. C. Presnall, & D. L. Anderson (Eds.) *Plates, plumes, and paradigms: Geological Society of America special paper*, (Vol. *388*, pp. 711–720).

Katz, R. F., Spiegelman, M., & Langmuir, C. H. (2003). A new parameterization of hydrous mantle melting. *Geochemistry, Geophysics, Geosystems*, *4*(9), 1073. https://doi.org/10.1029/2002gc000433

Kurosawa, K., & Genda, H. (2018). Effects of friction and plastic deformation in shock-comminuted damaged rocks on impact heating. *Geophysical Research Letters*, *45*(2), 620–626. https://doi.org/10.1002/2017GL076285

Kurosawa, K., Genda, H., Azuma, S., & Okazaki, K. (2021). The role of post-shock heating by plastic deformation during impact devolatilization of calcite ($CaCO_3$). *Geophysical Research Letters*, *48*(7), e2020GL091130. https://doi.org/10.1029/2020gl091130

Liu, T., Luther, R., Manske, L., & Wünnemann, K. (2022). Melt production and ejection from lunar intermediate-sized impact craters: Where is the molten material deposited? *Journal of Geophysical Research: Planets*, *127*(8), e2022JE007264. https://doi.org/10.1029/2022JE007264

Manske, L., Marchi, S., Plesa, A.-C., & Wünnemann, K. (2021). Impact melting upon basin formation on early Mars. *Icarus*, *357*, 114128. https://doi.org/10.1016/j.icarus.2020.114128

Manske, L., Wünnemann, K., & Kurosawa, K. (2022). Quantification of impact-induced melt production in numerical modeling revisited. TRR-170-DB. https://doi.org/10.35003/HVTJQD

Melosh, H. J. (1989). *Impact cratering: A geologic process*. Oxford University.

Melosh, H. J. (2007). A hydrocode equation of state for SiO_2. *Meteoritics & Planetary Science*, *42*(12), 2079–2098. https://doi.org/10.1111/j.1945-5100.2007.tb01009.x

Melosh, H. J., Ryan, E. V., & Asphaug, E. (1992). Dynamic fragmentation in impacts: Hydrocode simulation of laboratory impacts. *Journal of Geophysical Research*, *97*(E9), 14735–14759. https://doi.org/10.1029/92je01632

Moreau, J. G., Kohout, T., & Wünnemann, K. (2018). Melting efficiency of troilite-iron assemblages in shock-darkening: Insight from numerical modeling. *Physics of the Earth and Planetary Interiors*, *282*, 25–38. https://doi.org/10.1016/j.pepi.2018.06.006

Nakajima, M., Golabek, G. J., Wünnemann, K., Rubie, D. C., Burger, C., Melosh, H. J., et al. (2021). Scaling laws for the geometry of an impact-induced magma ocean. *Earth and Planetary Science Letters*, *568*, 116983. https://doi.org/10.1016/j.epsl.2021.116983

Ohnaka, M. (1995). A shear failure strength law of rock in the brittle-plastic transition regime. *Geophysical Research Letters*, *22*(1), 25–28. https://doi.org/10.1029/94gl02791

O'Keefe, J. D., & Ahrens, T. J. (1977). Impact-induced energy partitioning, melting, and vaporization on terrestrial planets. In *Lunar and planetary science conference proceedings* (Vol. *8*, pp. 3357–3374).

Pierazzo, E., & Melosh, H. J. (2000). Understanding oblique impacts from experiments, observations, and modeling. *Annual Review of Earth and Planetary Sciences*, *28*(1), 141–167. https://doi.org/10.1146/annurev.earth.28.1.141

Pierazzo, E., Vickery, A. M., & Melosh, H. J. (1997). A reevaluation of impact melt production. *Icarus*, *127*(2), 408–423. https://doi.org/10.1006/icar.1997.5713

Quintana, S. N., Crawford, D. A., & Schultz, P. H. (2015). Analysis of impact melt and vapor production in CTH for planetary applications. *Procedia Engineering*, *103*, 499–506. https://doi.org/10.1016/j.proeng.2015.04.065

Stöffler, D., Hamann, C., & Metzler, K. (2018). Shock metamorphism of planetary silicate rocks and sediments: Proposal for an updated classification system. *Meteoritics & Planetary Sciences*, *53*(1), 5–49. https://doi.org/10.1111/maps.12912

Thompson, S. L., & Lauson, H. S. (1972). *Improvements in the Chart D radiation-hydrodynamic CODE III: Revised analytic equations of state*. (No. SC-RR--71-0714). Sandia Labs.

Tonks, W. B., & Melosh, H. J. (1993). Magma ocean formation due to giant impacts. *Journal of Geophysical Research*, *98*(E3), 5319–5333. https://doi.org/10.1029/92je02726

Wakita, S., Genda, H., Kurosawa, K., & Davison, T. M. (2019). Enhancement of impact heating in pressure-strengthened rocks in oblique impacts. *Geophysical Research Letters*, *46*(23), 13678–13686. https://doi.org/10.1029/2019GL085174

Wakita, S., Genda, H., Kurosawa, K., Davison, T. M., & Johnson, B. C. (2022). Effect of impact velocity and angle on deformational heating and postimpact temperature. *Journal of Geophysical Research: Planets*, *127*(8), e2022JE007266. https://doi.org/10.1029/2022JE007266

Wünnemann, K., Collins, G. S., & Melosh, H. J. (2006). A strain-based porosity model for use in hydrocode simulations of impacts and implications for transient crater growth in porous targets. *Icarus*, *180*(2), 514–527. https://doi.org/10.1016/j.icarus.2005.10.013

Wünnemann, K., Collins, G. S., & Osinski, G. R. (2008). Numerical modelling of impact melt production in porous rocks. *Earth and Planetary Science Letters*, *269*(3–4), 530–539. https://doi.org/10.1016/j.epsl.2008.03.007

Zel'dovich, Y. B., & Raizer, Y. P. (1969). Shock waves and radiation. *Annual Review of Fluid Mechanics*, *1*(1), 385–412. https://doi.org/10.1146/annurev.fl.01.010169.002125